CMS Physics Analysis Summary

Contact: cms-pag-conveners-higgs@cern.ch 2015/08/22

Search for lepton-flavour-violating decays of the Higgs boson to eτ and eμ at $\sqrt{s} = 8$ TeV

The CMS Collaboration

Abstract

A direct search for lepton-flavour-violating decays of a Higgs boson (m_{H} = 125 GeV) is described. The search is performed for the $\mathrm{H} \to \mathrm{e}\tau_{\mu}$, $\mathrm{H} \to \mathrm{e}\tau_{h}$, and $\mathrm{H} \to \mathrm{e}\mu$ decays, where τ_{h} and τ_{μ} are taus reconstructed in the hadronic and muonic decay channels, respectively. The data sample used in the search corresponds to an integrated luminosity of 19.7 fb^{-1} collected in pp collisions at $\sqrt{s} = 8$ TeV with the CMS experiment at the CERN LHC. No evidence is found for lepton-flavour-violating decays in either final state. For the $\mathrm{H} \to \mathrm{e}\tau_{\mu}$ and $\mathrm{H} \to \mathrm{e}\tau_{h}$ channels, the sensitivity of the search is an order of magnitude better than the existing indirect limits. A constraint of $B(\mathrm{H} \to \mathrm{e}\tau) < 0.70\%$ at 95% confidence level is set. We also set a limit on the branching ratio of $B(\mathrm{H} \to \mathrm{e}\mu) < 0.036\%$ at 95% confidence level. The limits on $B(\mathrm{H} \to \mathrm{e}\tau)$ and $B(\mathrm{H} \to \mathrm{e}\mu)$ are subsequently used to constrain the $|Y_{\mathrm{e}\tau}|$ and $|Y_{\mathrm{e}\mu}|$ Yukawa couplings.

1 Introduction

The discovery of the Higgs boson (H) [1, 2] has generated great interest in exploring its properties. Within the Standard Model (SM), leptonic-flavour-violating (LFV) decays of the Higgs boson are forbidden [3]. Such decays can occur naturally in models with more than one Higgs doublet without abandoning renormalizability [4]. They also arise in supersymmetric models [5–7], composite Higgs models [8, 9], models with flavour symmetries [10], Randall-Sundrum models [11–13] and many others [14–19]. In the presence of LFV Higgs boson couplings, $\mu \to \mathrm{e}$, $\tau \to \mu$ and $\tau \to \mathrm{e}$ transitions proceed via a virtual Higgs boson [20, 21]. The experimental limits on these have recently been translated into constraints on $B(\mathrm{H} \to \mathrm{e}\mu, \mu\tau, \mathrm{e}\tau)$ [3, 22]. The null search results for $\mu \to \mathrm{e}\gamma$ [23] strongly constrains the $\mu \to \mathrm{e}$ transition: $B(\mathrm{H} \to \mathrm{e}\mu) < \mathcal{O}(10^{-8})$. However, the constraints on $\tau \to \mu$ and $\tau \to \mathrm{e}$ are much less stringent: $B(\mathrm{H} \to \mu\tau) < \mathcal{O}(10\%)$ and $B(\mathrm{H} \to \mathrm{e}\tau) < \mathcal{O}(10\%)$. These come from searches for $\tau \to \mu\gamma$ [24, 25] and other rare τ decays [26], $\tau \to \mathrm{e}\gamma$, muon and electron g-2 measurements. Exclusion limits on the electron and muon electric dipole moments [27] also provide complementary constraints. The direct searches for LFV Higgs boson decays at the LHC can improve significantly the limit on $B(\mathrm{H} \to \mathrm{e}\tau)$ and present an opportunity for discovering new physics.

To date no dedicated searches have been performed in the $\mathrm{H} \to \mathrm{e}\tau$ and $\mathrm{H} \to \mathrm{e}\mu$ channels. The Compact Muon Solenoid (CMS) collaboration has published a search in the $\mathrm{H} \to \mu\tau$ channels [28] in which a slight excess at $\mathrm{M_H} = 125\,\mathrm{GeV}$ is observed with a significance of 2.4σ. A constraint of $B(\mathrm{H} \to \mu\tau) < 1.51\%$ at 95% confidence level is set, while the best fit branching fraction is $B(\mathrm{H} \to \mu\tau) = (0.84^{+0.39}_{-0.37})\%$. Furthermore, a theoretical reinterpretation of the ATLAS $\mathrm{H} \to \tau\tau$ search results in terms of LFV decays by an independent group has been used to set limits at the 95% confidence level (CL) of $B(\mathrm{H} \to \mathrm{e}\tau) < 13\%$ [3].

This article describes a search for LFV decays of a Higgs boson with $\mathrm{M_H} = 125\,\mathrm{GeV}$ at the CMS experiment. The 2012 dataset recorded at $\sqrt{s} = 8$ TeV corresponding to an integrated luminosity of 19.7 fb^{-1} is used. The search is performed in three channels, $\mathrm{H} \to \mathrm{e}\tau_\mu$, $\mathrm{H} \to \mathrm{e}\tau_h$, and $\mathrm{H} \to \mathrm{e}\mu$, where τ_h and τ_μ are taus reconstructed in the hadronic and muonic decay channels, respectively. The final state signatures are very similar to the SM $\mathrm{H} \to \tau_\mathrm{e}\tau_h$ and $\mathrm{H} \to \tau_\mathrm{e}\tau_\mu$ decays, which have been studied by CMS in Ref. [29, 30], but with some significant kinematic differences. The electron in the $\mathrm{H} \to \mathrm{e}\tau$ decay comes promptly from the LFV Higgs boson decay and tends to have a larger momentum than in the SM case. For $\mathrm{H} \to \mathrm{e}\mu$, the Higgs boson candidate mass can be directly reconstructed with good resolution due to the absence of neutrinos and therefore there is negligible overlap with the corresponding SM $\mathrm{H} \to \tau_\mathrm{e}\tau_\mu$ search.

In the analysis of $\mathrm{H} \to \mathrm{e}\tau_\mu$ and $\mathrm{H} \to \mathrm{e}\tau_h$ decays, the two channels are divided into categories based on the number of jets in order to separate the different Higgs boson production mechanisms. The signal sensitivity is enhanced by using different selection criteria for each category. The dominant production mechanism is gluon gluon fusion (GGF) but there is also a significant contribution from vector boson fusion (VBF) which is enhanced by requiring jets to be present in the event. The dominant background in the $\mathrm{H} \to \mathrm{e}\tau_\mu$ channel is $\mathrm{Z} \to \tau_\mu\tau_\mathrm{e}$. Other much smaller backgrounds come from misidentified leptons in W+jets, QCD multijet and $\mathrm{t\bar{t}}$ events. In the $\mathrm{H} \to \mathrm{e}\tau_h$ channel the dominant background arises from misidentified τ leptons in W+jets, QCD multiple jet and $\mathrm{t\bar{t}}$ events. Less significant backgrounds come from $\mathrm{Z} \to \tau\tau$ and Z+jets. The principal backgrounds are estimated using data. There is also a small background from SM H decays which is estimated with simulation.

To improve the search sensitivity of the $\mathrm{H} \to \mathrm{e}\mu$ analysis, the events are divided into categories depending on the kinematics of the leptons and the number of jets. In this channel the sig-

nal is characterized by a narrow mass peak on top of a smooth background that is dominated by $t\bar{t}$ and WW leptonic decays. The reducible backgrounds cointaining at least one misidentified or nonisolated lepton are estimated using control samples. Furthermore, due to lepton identification cuts their impact on the analysis is highly reduced.

The presence or absence of signal is established using the asymptotic CL_s criterion [31, 32]. The selection was fixed and the agreement with observed data of relevant distributions was checked before looking in the mass region where the signal is expected.

After a description of the CMS detector (Sec. 2) and of the samples (Sec. 3), the event reconstruction is described in Sec. 4. The event selection and background components are described separately for the two channels in Sec. 5 and 6. The results are then presented in Sec. 7

2 CMS Detector

A detailed description of the CMS detector can be found elsewhere [33]. The momenta of charged particles are measured with a silicon pixel and strip tracker that covers the pseudorapidity range $|\eta| < 2.5$ and is in a 3.8 T axial magnetic field. The pseudorapidity is defined as $\eta = -\ln[\tan(\theta/2)]$, where θ is the polar angle of the trajectory of a particle with respect to the direction of the counterclockwise proton beam. Surrounding the tracker are a lead tungstate crystal electromagnetic calorimeter (ECAL) and a brass/scintillator hadron calorimeter (HCAL), both consisting of a barrel assembly and two endcaps that extend to a pseudorapidity range of $|\eta| < 3.0$. A steel/quartz-fiber Cherenkov forward detector extends the calorimetric coverage to $|\eta| < 5.0$. The outermost component of the CMS detector is the muon system, consisting of gas-ionization detectors placed in the steel return yoke of the magnet to measure the momenta of muons traversing through the detector. The two-level CMS trigger system selects events of interest for permanent storage. The first trigger level, composed of custom hardware processors, uses information from the calorimeters and muon detectors to select events in less than 3.2 μs. The high-level trigger software algorithms, executed on a farm of commercial processors, further reduce the event rate to 400 Hz using information from all detector subsystems.

3 Observed data and simulated samples

The data sample used for the analysis correspond to a total integrated luminosity of 19.7 fb^{-1} recorded in 2012. The trigger paths relevant for the $H \to e\tau_\mu$ and $H \to e\mu$ analysis require two well-identified different-flavour leptons. For the $H \to e\tau_h$ analysis, the relevant trigger paths are those requiring a single electron. More details are given in Sec. 5.1 and 6.1.

Simulated samples of signal and background events are produced using various event generators, with the CMS detector response modeled using GEANT4 [34]. The Higgs bosons are produced in proton-proton collisions predominantly by GGF, but also by VBF and in association with a W or Z boson. The $H \to e\tau$ decay samples are produced with PYTHIA 8.1 [35]. The $H \to e\mu$ decay samples are generated and simulated using PYTHIA 6.4 [36]. Several Higgs boson mass point samples have been produced for this channel: 115, 120, 125, 130, 140, and 150 GeV. The SM Higgs boson samples have been produced using POWHEG and PYTHIA 6. The production cross section has been set to 20.8 pb (for M_H=125 GeV) according to Ref. [37]. The MADGRAPH 5.1 [38] generator is used for $Z + jets$, $W + jets$, $t\bar{t}$, and diboson production, and POWHEG for single-top-quark production. The POWHEG and MADGRAPH generators are interfaced with PYTHIA for parton shower and fragmentation. The PYTHIA parameters for the

underlying event description are set to the Z2* tune. Due to the high luminosities attained during the run many events have multiple proton-proton interactions per bunch crossing (pileup). All simulated samples are reweighted to match the true pileup distribution in the observed data by applying an event weight based on the number of simulated pileup events and the instantaneous luminosity per bunch-crossing averaged over the run period considered.

4 Event Reconstruction

A particle flow (PF) algorithm [39–41] combines the information from all CMS sub-detectors to identify and reconstruct the individual particles emerging from all vertices: charged hadrons, neutral hadrons, photons, muons, and electrons. These particles are then used to reconstruct the missing transverse energy ($E_{\mathrm{T}}^{\mathrm{miss}}$), jets, hadronic τ decays, and to quantify the isolation of leptons and photons. The variable $\Delta R = \sqrt{(\Delta\eta)^2 + (\Delta\phi)^2}$ is used to measure the separation between reconstructed objects in the detector, where ϕ is the azimuthal angle (in radians) of the trajectory of the object in the plane transverse to the direction of the proton beams.

The large average pileup in 2012 (21 interactions per bunch crossing) makes the identification of the vertex corresponding to the hard-scattering process nontrivial. This affects most of the physics objects: jets, lepton isolation, etc. The tracking system is able to separate collision vertices as close as 0.5 mm along the beam direction [42]. For each vertex, the sum of the p_{T}^2 of all tracks associated with the vertex is computed. The vertex for which this quantity is the largest is assumed to correspond to the hard-scattering process, and is referred to as the primary vertex in the event reconstruction.

Muons are selected among the reconstructed candidates obtained from a global track fit seeded by the track segment in the muon system and taking into account compatibility with small energy deposits in the calorimeters. Identification is performed applying selections based on track quality and isolation. The muon momentum is measured by the combination of the measurement in the inner tracker detector and the outer muon chambers. The bias in the reconstructed muon p_{T} is determined from the position of the Z mass peak as a function of muon kinematic variables, and a correction is derived according to the procedure outlined in [43].

Electron reconstruction requires the matching of an energy cluster in the ECAL with a track in the silicon tracker. Identification criteria based on the ECAL shower shape, matching between the track and the ECAL cluster, and consistency with the primary vertex are imposed. Electron identification relies on a multivariate technique that combines observables sensitive to the amount of bremsstrahlung along the electron trajectory, the geometrical and momentum matching between the electron trajectory and associated clusters, as well as shower-shape observables. Additional requirements are imposed to remove electrons produced by photon conversions. The electron energy is measured using the electron boosted-decision-tree (BDT) regression as in the $\mathrm{H} \to \mathrm{ZZ}$ analysis [44].

Jets misidentified as electrons are suppressed by the isolation requirements. An isolation sum is calculated as follows:

$$Iso = \frac{\sum PFChIso(e) + max(0., PFPhoIso(e) + PFNeuIso(e) - A_{eff} \cdot \rho)}{p_{\mathrm{T}}(e)} \quad (1)$$

where PFChIso is the scalar sum of the transverse momenta of charged hadron tracks which are consistent with originating from the primary vertex and lie within a hollow cone of size $\Delta R = 0.3$ centered around lepton direction, PFPhoIso is computed as the transverse energy

sum of PF photons located within a cone of size $\Delta R = 0.3$, centered around the lepton position, excluding an inner veto cone and η-slice in order to exclude the footprint of the candidate and PFNeuIso is the sum of the energies of neutral hadrons whose centres lie within a cone of outer radius $\Delta R = 0.3$ centered on lepton direction. For each of the isolation sums defined above, the energy deposited within the isolation cone is contaminated by energy from pile-up and from the underlying event. Since the contamination increases with the number of pile-up vertices (nPV), the efficiency of the isolation cut decreases with increasing pile-up. In order to maintain high efficiency under high pile-up conditions, the contribution to the isolation from pile-up and the underlying event is estimated on an event-by-event basis as the product of the measured energy density ρ for the event, determined using the FASTJET algorithm [45], and an effective area A_{eff} corresponding to the isolation cone excluding veto regions.

Jets are reconstructed from all the PF particles using the anti-k_t jet clustering algorithm [46] implemented in FASTJET, with a distance parameter of $R = 0.5$. The jet energy is corrected to unify response in the detector [47]. An additional correction takes into account the contribution of particles created in pileup interactions and in the underlying event. Particles from different pileup vertices can be clustered into a pileup jet, or significantly overlap a jet from the primary vertex below the p_T threshold applied in the analysis. Such jets are identified and removed [48].

Hadronically decaying τ leptons are reconstructed and identified using the hadron plus strips (HPS) algorithm [49] which targets the main decay modes by selecting PF candidates with one charged hadron and up to two neutral pions, or with three charged hadrons. A photon from a neutral-pion decay can convert in the tracker material into an electron and a positron, which can then radiate bremsstrahlung photons. These particles give rise to several ECAL energy deposits at the same η value and separated in azimuthal angle, and are reconstructed as several photons by the PF algorithm. To increase the acceptance for such converted photons, the neutral pions are identified by clustering the reconstructed photons in narrow strips along the azimuthal (ϕ) direction. Hadronic taus reconstructed by the HPS algorithm are required to be isolated in order to suppress misidentification of quark and gluon jets. The isolation is defined as the sum of the p_T of all the charged hadrons and of the E_T of all the photons in a cone of $\Delta R = 0.5$ around the τ. The neutral component is corrected to mitigate the effect of the pileup. In addition, dedicated discriminators against electrons and muons are applied to the τ candidate.

The missing transverse energy, E_T^{miss}, is defined as the magnitude of the negative of the vector sum of the transverse momenta of all identified PF objects in the events.

5 $H \rightarrow e\tau$

5.1 Event Selection

The $H \rightarrow e\tau_h$ channel selection begins by requiring an event recorded with a single electron trigger with a transverse momentum threshold p_T of 27 GeV in the pseudo-rapidity range $|\eta| < 2.5$, while the $H \rightarrow e\tau_\mu$ channel requires a muon-electron trigger with p_T thresholds of 17 GeV ($|\eta| < 2.5$) for the electron and 8 GeV ($|\eta| < 2.4$) for the muon. Loose electron and muon identification criteria are applied at the trigger level. The leptons are also required to be isolated from other tracks and calorimeter energy deposits to maintain an acceptable trigger rate.

The event selection continues with three additional steps. First a loose selection defining the basic signature is applied. The sample is then divided into categories according to the number

of jets in the event. Finally, requirements are placed on a set of kinematic variables designed to suppress the backgrounds.

The loose selection for the $H \to e\tau_\mu$ channel requires an isolated muon ($p_T^\mu > 10$ GeV, $|\eta| < 2.1$) and an isolated electron ($p_T^e > 40$ GeV, $|\eta| < 2.3$) of opposite charge lying within a region of the detector that allows good identification. The electron and muon are required to be separated by $\Delta R > 0.1$. The $H \to e\tau_h$ channel requires an isolated electron ($p_T > 30$ GeV, $|\eta| < 2.3$) and an isolated hadronically decaying τ ($p_T^{\tau_h} > 30$ GeV, $|\eta| < 2.3$) of opposite charge. Leptons are also required to be isolated from any jet in the event with $p_T > 30$ GeV by $\Delta R > 0.4$.

The events are then divided into categories within each channel according to the number of jets in the event. Jets are required to pass identification criteria, have $p_T > 30$ GeV and lie within the range $|\eta| < 4.7$. The zero-jet category contains events primarily produced by GGF. The one-jet category predominantly contains events produced by GGF and a negligibly small number of events produced in association with a W or Z boson decaying hadronically. The categories with two jets are designed to enhance the selected events with those produced via the VBF process.

The main variable for the discrimination between the signal and the background is the collinear mass, M_{col}, which provides an estimator of the reconstructed Higgs boson mass using the observed decay products. This is constructed using the collinear approximation [50] which is based on the observation that since the mass of the Higgs boson is much greater than the mass of τ, the τ decay products are highly boosted in the direction of the τ. Thus the neutrino momenta can be approximated to be in the same direction as the other visible decay products of the τ. Hence the component of the E_T^{miss} in the direction of the visible τ decay products is used to estimate the transverse component of the neutrino momentum:

$$\vec{p}_T^{\,\nu} = \vec{E}_T^{\,miss} \cdot \hat{p}_T^{\,\tau_{vis}}.$$

The fraction of the τ momentum carried by the visible τ decay products, $x_{\tau_{vis}}$, is given by:

$$x_{\tau_{vis}} = \frac{|\vec{p}_T^{\,\tau_{vis}}|}{|\vec{p}_T^{\,\tau_{vis}}| + |\vec{p}_T^{\,\nu}|}.$$

The τ four momentum is then $(x_{\tau_{vis}}|\vec{p}^{\,\tau_{vis}}|, x_{\tau_{vis}}\vec{p}^{\,\tau_{vis}})$ and since $M_H \gg m_\tau, m_l$:

$$M_H = M_{col} = \frac{M_{vis}}{\sqrt{x_{\tau_{vis}}}}.$$

Figure 1 shows M_{col} distribution of observed data and simulated backgrounds for each of the categories in each channel after the loose selection. The simulated signal for $B(H \to e\tau) = 100\%$ is shown. The principal backgrounds are estimated with data using techniques described in Sec. 5.2. There is good agreement between the observed distribution and that of the background estimation. The agreement is similar in all of the kinematic variables that are subsequently used to suppress backgrounds. The analysis was performed "blinded", i.e. fixing the selection and checking the observed data-simulation agreement of relevant distributions outside the mass region $100 < M_{col} < 150$ GeV.

Next, a set of kinematic variables is defined and the criteria for selection is determined by optimizing for $S/\sqrt{S+B}$ where S and B are the expected signal and background event yields in the mass window $100 < M_{col} < 150$ GeV. The signal event yield corresponds to the SM Higgs boson production cross-section at $M_H = 125$ GeV with $B(H \to e\tau) = 1\%$. The criteria for

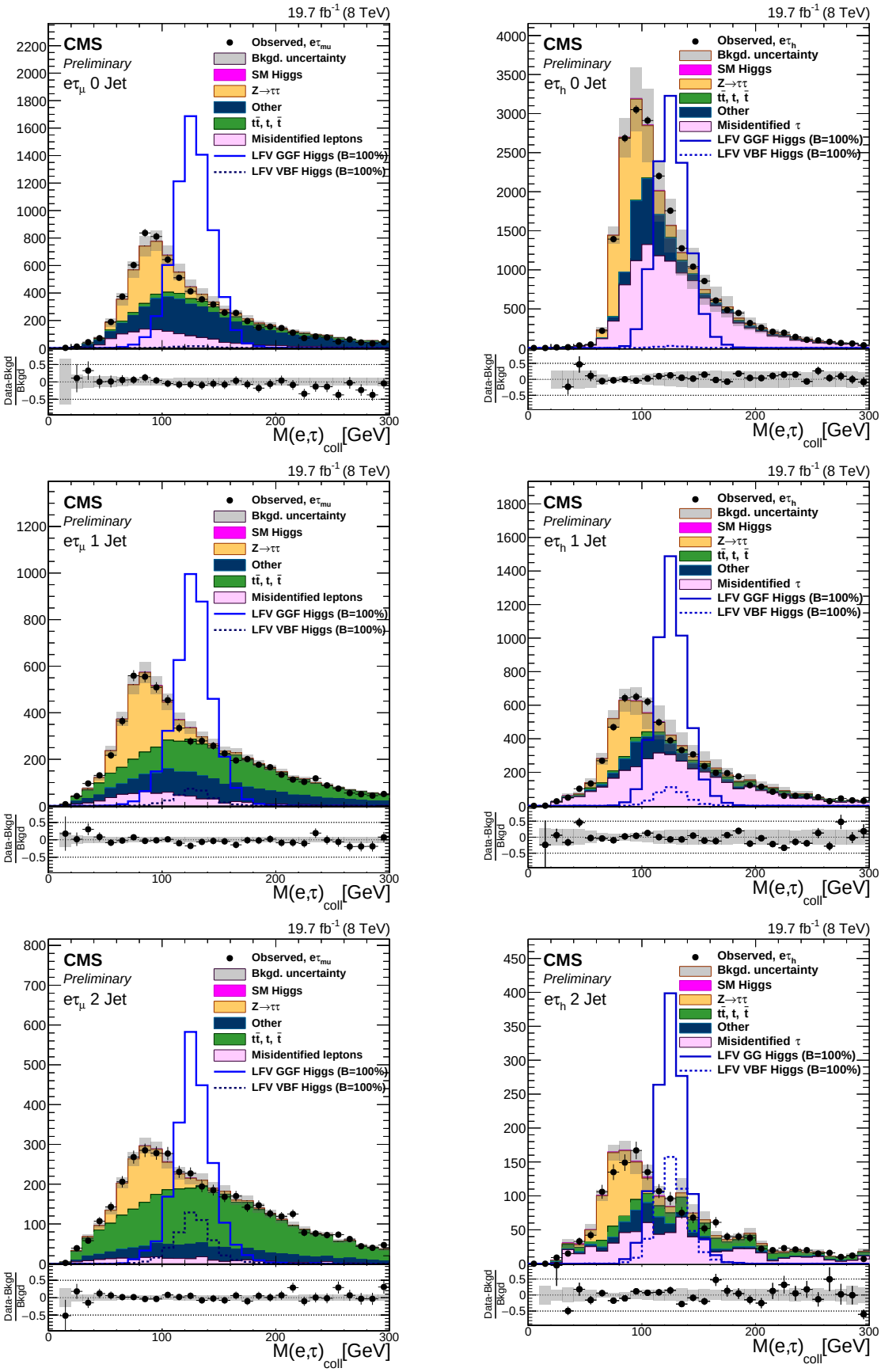

Figure 1: Comparison of the observed collinear mass distributions with the background expectations after the loose selection requirements. The shaded gray bands indicate the total uncertainty. The expected distributions for signal with $B(H \to e\tau) = 100\%$ are shown for clarity. Top left: $H \to e\tau_\mu$ 0-jet; top right: $H \to e\tau_h$ 0-jet; middle left: $H \to e\tau_\mu$ 1-jet; middle right: $H \to e\tau_h$1-jet; bottom left: $H \to e\tau_\mu$ 2-jet; bottom right $H \to e\tau_h$ 2-jet.

Table 1: Selection criteria requirements for the kinematic variables after the loose selection.

Variable		$H \to e\tau_\mu$			$H \to e\tau_h$		
		0-jet	1-jet	2-jet	0-jet	1-jet	2-jet
p_T^e	(GeV)	> 50	> 40	> 40	> 45	> 35	> 35
p_T^μ	(GeV)	> 15	> 15	> 15	-	-	-
$p_T^{\tau_h}$	(GeV)	-	-	-	> 30	> 40	> 30
$M_T(\mu)$	(GeV)	-	< 30	< 40	-	-	-
$M_T(\tau_h)$	(GeV)	-	-	-	< 70	-	< 50
$\Delta\phi_{\vec{p}_{T,e}-\vec{p}_{T,\tau_h}}$	(radians)	-	-	-	> 2.3	-	-
$\Delta\phi_{\vec{p}_{T,\mu}-\vec{E}_{\mathrm{T}}^{\mathrm{miss}}}$	(radians)	< 0.8	< 0.8	-	-	-	-
$\Delta\phi_{\vec{p}_{T,e}-\vec{p}_{T,\mu}}$	(radians)	-	> 0.5	-	-	-	-

each category, and in each channel, are given in Table 1. The variables used are the transverse momenta of the τ, muon, and electron; azimuthal angles between the leptons; azimuthal angles between the leptons and the transverse missing energy vectors; the transverse mass. The transverse mass is constructed from the transverse missing energy vector $\vec{E}_{\mathrm{T}}^{\mathrm{miss}}$ and the lepton tranverse momentum $\vec{p_{\mathrm{T}}}(l)$ as follows:

$$M_T(\ell) = \sqrt{2p_T(\ell)E_{\mathrm{T}}^{\mathrm{miss}}(1-\cos\Delta\phi_{\vec{p}_T(l)-\vec{E}_{\mathrm{T}}^{\mathrm{miss}}})}$$

where $\Delta\phi_{\vec{p}_T(l)-\vec{E}_{\mathrm{T}}^{\mathrm{miss}}}$ is the azimuthal angle between the missing energy and the lepton momentum. Events in which at least one of the jets is identified as coming from a b-quark decay are vetoed using the combined secondary-vertex b-tagging algorithm [51]. Events in the VBF category are additionally required to have two jets separated by a rapidity gap ($|\Delta\eta| > 2.3$) and to have a dijet invariant mass greater than 400 GeV in the H $\to$ eτ_h channel. In the H $\to$ eτ_μ channel the requirements have been set to $|\Delta\eta| > 3$ and 200 GeV.

5.2 Background processes

The contribution of the dominant background processes are estimated using data while the less significant backgrounds are estimated using simulation. The largest backgrounds come from Z $\to \tau\tau$ decays and from jets misidentified as leptons in W+jets and QCD multijet production.

5.2.1 $Z \to \tau\tau$

The $Z \to \tau\tau$ background contribution is estimated using an embedding technique [30, 52]. Firstly, a sample of $Z \to \mu\mu$ events is selected from data using a loose muon selection. The muons are then replaced with simulated τ decays reconstructed with the particle flow algorithm. Thus, the key features of the event topology such as the jets, missing energy and underlying event are taken directly from data with only the τ decays being simulated. The normalization of the sample is obtained from the simulation. The technique is validated by comparing the collinear mass distributions obtained from the $Z \to \tau\tau$ simulation and the embedded technique. A shift of 2% of the mass peak of the embedded sample with respect to simulation is observed. This shift corrects a bias in the embedding technique, which does not take final state radiation photons into account. Identification and isolation corrections derived by the comparison are applied to the embedded sample.

5.2.2 Misidentified leptons

Leptons can arise from misidentified jets in W+jets and QCD multijet processes. This background is estimated using a method based on data. It is employed slightly differently in the

$H \to e\tau_\mu$ and $H \to e\tau_h$ channels. The technique is shown schematically in Table 2. The difference in the two channels is how the selection requirements ($S(\ell)$) are altered to define regions III and IV. In $H \to e\tau_\mu$ region I is the signal region in which an isolated muon and an isolated electron is required.

Region III is a data sample in which all the analysis selection criteria are applied except that the muon is required to be not isolated ($S'(\ell)$). These samples are dominated by W+jets

Table 2: Schematic to illustrate the application of the method used to estimate the misidentified lepton (ℓ) background. Samples are defined by the charge of the two leptons and by the isolation requirements on each. Charged conjugates are assumed.

Region I	**Region II**
ℓ_1^+(isolated)	ℓ_1^+(isolated)
ℓ_2^-(isolated)	ℓ_2^+(isolated)
Region III	**Region IV**
ℓ_1^+(isolated)	ℓ_1^+(isolated)
ℓ_2^-(not-isolated)	ℓ_2^+(not-isolated)

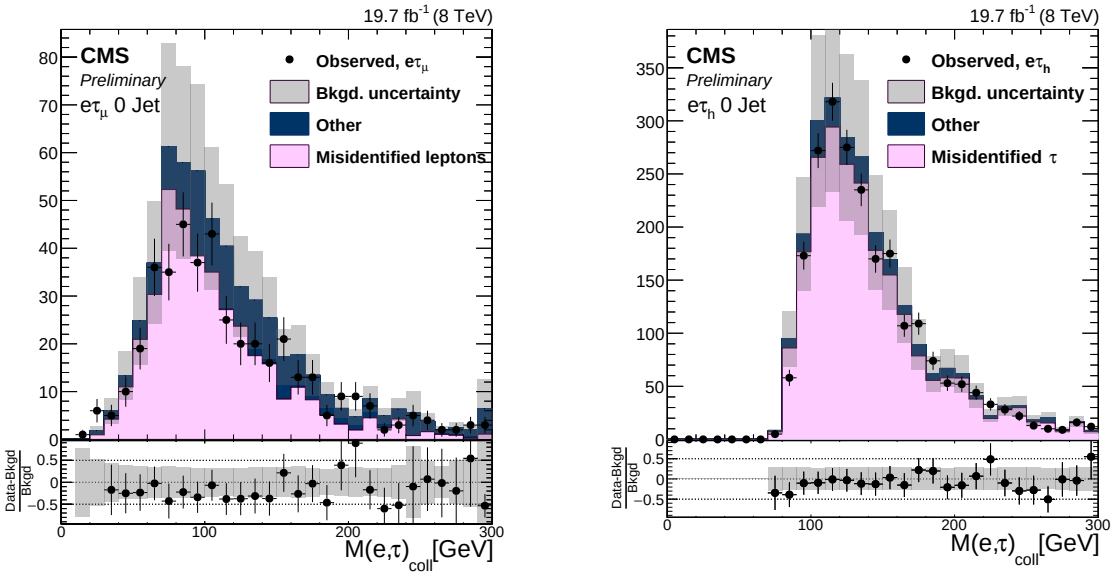

Figure 2: Distributions of M_{col} for region II. Left: $H \to e\tau_\mu$. Right: $H \to e\tau_h$.

and QCD multijet events but with small backgrounds from WW, ZZ that are subtracted using simulation expectations. The misidentified muon background in region I is then estimated by multiplying the event yield in region III by a factor f_μ, where f_μ is the ratio of not isolated to isolated muons. It is computed in an independent data sample $Z \to \mu\mu + X$, where X is an object identified as a muon, in bins of muon p_T and η. Due to the high p_T electron threshold, the misidentified electron background is negligible in comparison to the misidentified muon background and the small backgrounds from WW and ZZ, therefore only misidentified muons have to be considered. The technique is validated by using observed like-sign lepton data from the regions II and IV shown schematically in Table 2. In Figure 2 the observed data events are compared to simulation in the like sign control region. The agreement is good.

In the $H \to e\tau_h$ channel, both the τ_h and the electron candidate can come from a misidentified jet from a number of sources, predominantly W+jets and QCD multijet events, but also

$Z \to ee$+jets and $t\bar{t}$. The misidentification rate f_τ is defined as the fraction of τ_h candidates with a loose isolation that also pass a tight isolation requirement. It is measured in observed $Z \to ee + X$ events, where X is an object identified as a τ. The misidentification rate measured in $Z \to ee + X$ data is checked by comparing to that measured in $Z \to ee + X$ simulation and found to be in good agreement. The measured misidentification rate is then used as previously described, and illustrated schematically in Table 2. In this case region I, the signal region, is the baseline event selection with both an isolated τ and an isolated electron. Region III comprises the baseline selection with an isolated electron and a loose but not tight isolated τ requirement. This region is dominated by W+jets and QCD multijet background and there is good agreement between the observed and the expected yields from simulation. The misidentified τ number in Region I is estimated by multiplying the event yield in Region III by a factor $f_\tau/(1-f_\tau)$. The same procedure is applied for electrons, the number of misidentified electrons is estimated by multiplying the event yield in Region III by a factor $f_e/(1-f_e)$. To avoid double counting, the event yield in Region III multiplied by a factor $f_e/(1-f_e) \times f_\tau/(1-f_\tau)$ is subtracted to the sum of misidentified electrons and taus. The procedure can be validated with like sign $e\tau$ events. Figure 2 shows the good agreement between observed data and simulation for the like sign samples.

The method assumes that the misidentification rate in $Z \to ee + X$ events is the same as for W+jets and QCD processes. To test this assumption the misidentification rates are measured in a QCD jet data control sample. They are found to be consistent.

5.2.3 Other Backgrounds

The leptonic decay of W bosons produced in top decays from $t\bar{t}$ pairs produces opposite sign di-leptons and E_T^{miss}. This background is estimated using simulated $t\bar{t}$ events using the shape of the M_{col} distribution from simulation and a data control region for normalization. The control region is the 2-jet selection but with the additional requirement that at least one of the jets is b-tagged in order to enhance the $t\bar{t}$ contribution.

Other smaller backgrounds come from WW, ZZ+jets, Wγ+jets and single top-quark production. Each of these is estimated with simulation.

5.3 Systematic uncertainties

To set upper bounds on the signal strength μ, or determine a signal significance, we use the CL_s method [31, 32]. A binned likelihood is used, based on the distributions of M_{col} for the signal and the various background sources. Systematic uncertainties are represented by nuisance parameters, some of which only affect the background and signal normalizations, and others which affect the shape and/or normalization of the M_{col} distributions.

5.3.1 Normalization uncertainties

The uncertainties are summarized in Tables 3 and 4. The uncertainties in the electron and muon selection efficiencies (trigger, identification and isolation) are estimated using the tag and probe technique in observed $Z \to \mu\mu$, ee data [52]. The identification efficiency of hadronic τ is estimated using tag and probe in observed $Z \to \tau\tau$ events [49]. The uncertainty in the $Z \to \tau\tau$ background comes predominantly from the uncertainty in the τ identification efficiency. The uncertainties in the estimation of the misidentified lepton rate come from the difference in rates measured into different data samples (QCD multijet and W+jets). The uncertainty in the production cross section of the backgrounds that have been estimated by simulation is also included.

Table 3: Systematic uncertainties on the expected yield in % for the $e\tau_h$ and $e\tau_\mu$ channels. All uncertainties are treated as correlated between the categories, except if there are two values quoted. In this case the number denoted with * is treated as uncorrelated between categories.

Systematic	$H\to e\tau_h$			$H\to e\tau_\mu$		
	0–jet	1–jet	2–jet	0–jet	1–jet	2–jet
Electron Trigger/ID/Isolation	1	1	2	3	3	3
Muon Trigger/ID/Isolation	-	-	-	2	2	2
Hadronic tau efficiency	6.7	6.7	6.7	-	-	-
Luminosity	2.6	2.6	2.6	2.6	2.6	2.6
B-Tagging veto	-	-	-	3	3	3
$Z \to \tau\tau$ background	$3 \oplus 5^*$	$3 \oplus 5^*$	$3 \oplus 10^*$	$3 \oplus 5^*$	$3 \oplus 5^*$	$3 \oplus 10^*$
$Z \to \mu\mu$, ee background	30	30	30	30	30	30
Reducible background	30	30	30	40	40	40
Diboson background	15	15	15	15	15	15
Top pair background	10	10	$10 \oplus 33^*$	10	10	$10 \oplus 10^*$
Single top background	10	10	10	10	10	10
Higgs boson GGF production	$9.7 \oplus 4 \oplus 8$					
Higgs boson VBF production	$3.6 \oplus 10 \oplus 4$					

There are several theoretical uncertainties on the Higgs boson production cross section, which depend on the production mechanism and the analysis category. They are given in Table 4. Note that these enter both for the LFV Higgs boson and the SM Higgs boson background and are treated as 100% correlated. The parton distribution function (PDF) uncertainty is evaluated by comparing the yields in each category, when spanning the recommended parameter range of a number of different independent PDF sets including CT10 [53], MSTW [54], NNPDF [55] and following PDF4LHC [56] recommendation. The scale uncertainty is estimated by varying the renormalization, μ_R, and factorization, μ_F, scales high and low by one half or two times the nominal scale under the constraint $0.5 < \mu_F/\mu_R < 2$. The underlying event and parton shower uncertainty is estimated by using two different PYTHIA tunes. Anticorrelations arise due to migration of events between the categories and are expressed as negative numbers.

Table 4: Theoretical uncertainties in % for Higgs boson production cross section. Anticorrelations arise due to migration of events between the categories and are expressed as negative numbers.

Systematic Uncertainty	Gluon-Gluon Fusion			Vector Boson Fusion		
	0-jet	1-jet	2-jet	0-jet	1-jet	2-jet
Parton distribution function	+9.7	+9.7	+9.7	+3.6	+3.6	+3.6
Renormalization scale	+8	+10	−30	+4	+1.5	+2
Underlying event/parton shower	+4	−5	−10	+10	<1	−1

5.3.2 M_{col} shape uncertainties

The systematic uncertainties that lead to a change in the shape of the M_{col} distribution are summarized in Table 5.

In the embedded $Z \to \tau\tau$ M_{col} distribution used to estimate the $Z \to \tau\tau$ background, a 2% shift has been observed with respect to $Z \to \tau\tau$ simulations by comparing the means of both dis-

Table 5: Systematic uncertainties in the shape of the signal and background templates, expressed in %

Systematic	$H \to e\tau_\mu$	$H \to e\tau_h$
Hadronic tau energy scale	-	3
Jet energy scale	3-7	3-7
Unclustered energy scale	10	10
$Z \to \tau\tau$ bias	2 ± 2	-
$Z \to$ ee bias	-	5

tributions. This occurs only in the H $\to$ eτ_μ channel. The template has been corrected for this effect and a 100% uncertainty on this shift is used. For the $Z \to$ ee background in the hadronic channel a systematics uncertainty of 5% has been considered to account for the mismeasured energy of the electron reconstructed as a τ. This uncertainty has been extracted from a comparison of the observed data with simulation in a control region obtained by inverting the anti-electron discriminator requirement in the τ identification. The jet energy scale has been studied extensively by the CMS collaboration and a standard prescription for corrections is used in all analyses [47]. The uncertainties are applied as a function of p_T and η including all correlations. The overall scale is set using $\gamma +$ jets events and the most significant uncertainty arises from the photon energy scale. A number of other uncertainties such as jet fragmentation modeling, single pion response and uncertainties in the pileup corrections are also included. The jet energy scale uncertainty is propagated to the missing energy. There is also an additional uncertainty to account for the unclustered energy scale uncertainty. The unclustered energy comes from jets below 10 GeV and particle flow candidates not within jets. It is also propagated to the missing energy. The τ energy scale is estimated by comparing Z $\to \tau\tau$ events in observed data and simulation. Good agreement is found and a 3% uncertainty is assigned. Finally, the M_{col} distributions used in the fit have a statistical uncertainty in each mass bin that is included as an uncertainty that is uncorrelated between the bins.

Potential uncertainties in the shape of the misidentified lepton backgrounds have also been considered. In the H $\to$ eτ_μ channel the misidentified lepton rates are applied in bins of p_T and η. These rates are adjusted all up or down by one standard deviation (σ) and the differences in the shapes are then used as nuisance parameters in the fit. In the H $\to$ eτ_h channel the τ lepton misidentification rate was found to be approximately flat in p_T but to depend on η. The uncertainty of the parametrized misidentification rate as function of η is propagated to obtain the modified shapes to be used as systematics in the fit.

6 H $\to$ eμ

6.1 Event Selection

The first step of the event selection is the trigger requirement: two well-identified different flavour leptons with 17 and 8 GeV p_T thresholds. To improve the search sensitivity, the sample is split into different categories. Two dijet categories are defined, aimed at selecting events produced in the VBF process. The jet selection of these two categories is the same as in the H $\to \gamma\gamma$ analysis [57]. The rest of the events are classified into nine categories according to lepton kinematics and number of jets (number of non-pileup jets with $p_T > 20$ GeV). The definition of the categories is summarized in Table 6. The splitting between barrel and endcaps is different between electrons and muons and it reflects the boundaries of ECAL, tracker, and

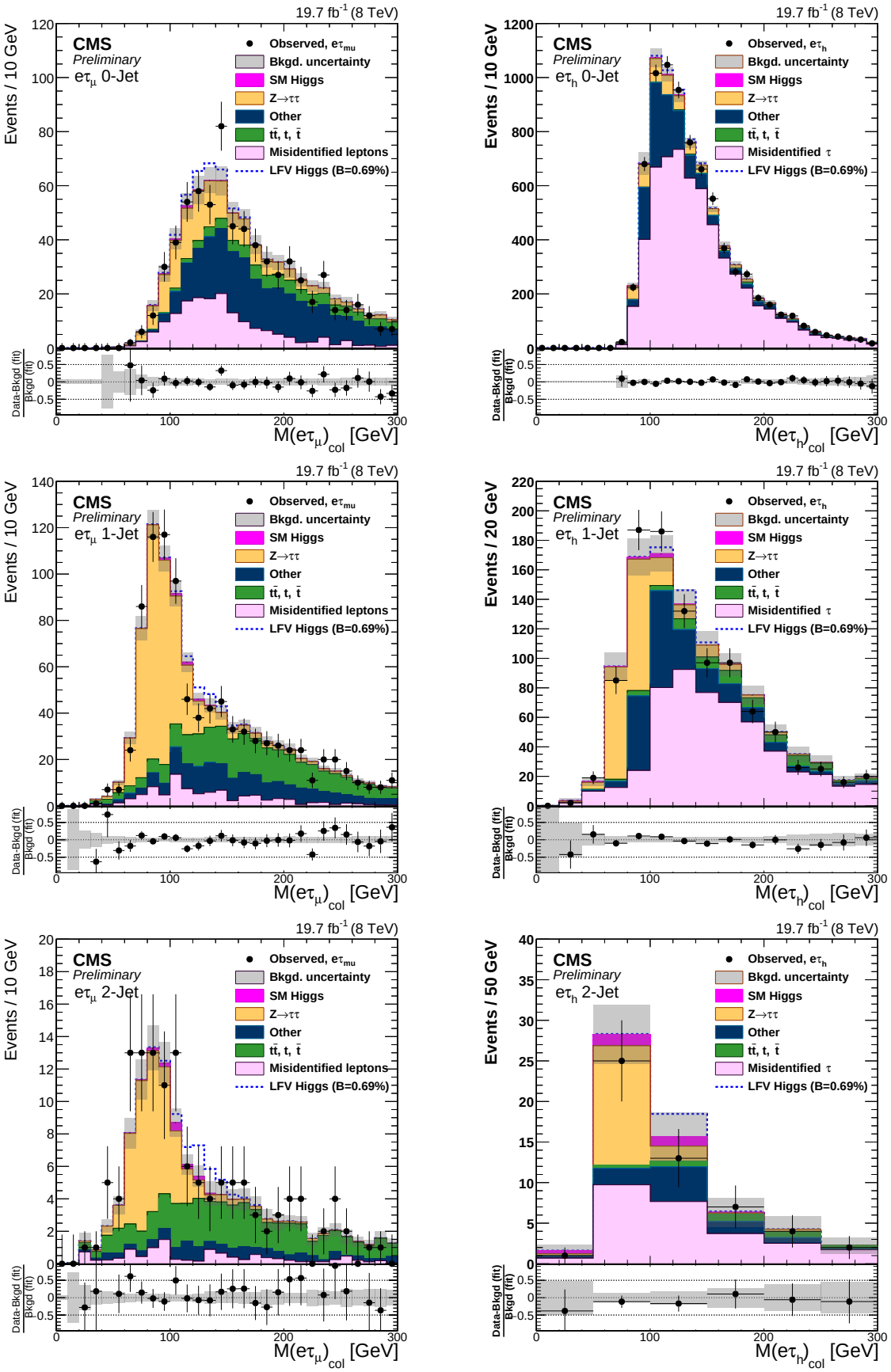

Figure 3: Comparison of the observed collinear mass distributions with the background expectations after the fit. The simulated distributions for signal is shown for the branching ratio $B(H \to e\tau) = 0.69\%$. Top left: $H \to e\tau_\mu$ 0-jet; top right: $H \to e\tau_h$ 0-jet; middle left: $H \to e\tau_\mu$ 1-jet; middle right: $H \to e\tau_h$1-jet; bottom left: $H \to e\tau_\mu$ 2-jet; bottom right $H \to e\tau_h$ 2-jet.

muon detectors and the differences in mass resolution.

The following additional criteria are applied: a selection on the maximum $E_{\mathrm{T}}^{\mathrm{miss}}$ value, computed to particle flow candidates, to reduce the contribution of background with genuine missing transverse energy (e.g. WW), an anti-btag (upper) selection on the CSV discriminant [58] to largely reduce the $\mathrm{t\bar{t}}$ background, an upper cut on the electron isolation variable at 0.2 and a lower cut on the electron identification variable at 0.8.

Events with more than two jets are not considered. Scaling factors due to imperfect modeling of the b-tag efficiencies are applied by reweighting signal events.

The selection has been optimized to maximize signal-to-background ratio in each category separately using simulated events with the same composition described in the introduction of this paper. Table 6 summarizes the optimized cuts for each of the categories used in the analysis.

Table 6: Selection criteria for each of the categories used in this analysis. The EB-MB (ME) categories include only events with the electron in the calorimeter barrel $|\eta_e| < 1.479$ and the muon in the muon detector barrel (endcap) $|\eta_\mu| < 0.8$ ($|\eta_\mu| > 0.8$). In the EE-(MB or ME) categories the electron is required to be in the calorimeter endcap ($|\eta_e| < 1.566$), while no selection is applied to the muon pseudorapidity.

Category		Number of jets	Lepton p_{T} (GeV)	$E_{\mathrm{T}}^{\mathrm{miss}}$ (GeV)	B-tag
0	EB-MB	0	> 25	< 30	-
1	EB-MB	1	> 22	< 30	< 0.38
2	EB-MB	2	> 25	< 25	$< 0.38, < 0.48$
3	EB-ME	0	> 20	< 30	-
4	EB-ME	1	> 22	< 20	< 0.48
5	EB-ME	2	> 20	< 30	$< 0.51, < 0.57$
6	EE-(MB or ME)	0	> 20	< 30	-
7	EE-(MB or ME)	1	> 22	< 20	< 0.48
8	EE-(MB or ME)	2	> 20	< 30	$< 0.51, < 0.57$
VBF					
9	Tight	2	> 22	< 30	$< 0.58, < 0.244$
10	Loose	2	> 22	< 25	$< 0.62, < 0.30$

6.2 Signal and Background modelling

6.2.1 Background Model

The background is fitted from data over the mass range 110 to 160 GeV. Because we do not have an analytical model of the background, we select the background parametrization from several groups of 'simple' analytical functions: polynomials, sums of exponentials and sums of power law functions.

The background functions are used as models to generate 10000 samples (toys). A small amount of signal (corresponding to a branching ratio of 10^{-3}) is added to avoid problems when negative values of the signal strength are evaluated during the fits. Several functions from each family (chosen to start with order of the generating function) are then fitted to each of these toys and the bias (defined as fitted signal strength minus injected signal strength) is determined. For each fitting function, the median bias is determined and the largest value over any generating function and simulated signal mass point is considered. For each category, the lowest-order function with a bias below the threshold of 14% is then selected, as shown in Table 7.

Table 7: Selected functions and orders for background model in each category.

Category	Selected function	Selected order	Bias
0	Polynomial	4	10.8 ± 1.0 %
1	Polynomial	4	4.6 ± 1.1 %
2	Power law	1	7.6 ± 1.0 %
3	Polynomial	4	4.8 ± 1.1 %
4	Exponential	1	7.4 ± 1.0 %
5	Exponential	1	8.4 ± 1.0 %
6	Polynomial	4	13.8 ± 1.4 %
7	Power law	1	12.6 ± 1.0 %
8	Polynomial	4	7.7 ± 1.1 %
9	Exponential	1	< 0.1 %
10	Exponential	1	< 0.1 %

Table 8: Systematic uncertainties on the expected yield for the $H \to e\mu$. All uncertainties have been considered as correlated between categories.

Experimental uncertainties	
Jet energy scale (inclusive categories)	0.6% - 22.4 %
Jet energy scale (VBF categories)	0.1% - 77.6 %
Jet energy resolution (inclusive categories)	0.3% - 23.8 %
Jet energy resolution (VBF categories)	8.4% - 93.7 %
Luminosity	2.6%
Trigger efficiency	1.0%
Lepton ID	2.0%
Leton energy scale	1.0%
Di-lepton mass resolution	5.0%
Pileup	0.7% - 2.3 %
B-tag efficiency	0.05 % - 0.70 %
Acceptance (PDF variations)	0.8 % - 5.1 %
Theoretical uncertainties	
GGF cross section (QCD scale)	+7.2/-7.8%
GGF cross section (PDF+α_s)	+7.5/-6.9%
VBF cross section (QCD scale)	$\pm$0.2%
VBF cross section (PDF+α_s)	+2.6/-2.8%

6.2.2 Signal Model

In order to statistically interpret the observed data, it is necessary to have a description of the signal which specifies the overall product of efficiency and acceptance. The simulated signal is used, after the smearing of the resolution and the application of all efficiency corrections and scale factors, to a fit sum of two Gaussians in each selection category and production mechanism (GGF and VBF).

6.3 Systematic uncertainties

Since we fit the background from the data (see Section 6.2), we only consider systematic uncertainties affecting the signal. These uncertainties are summarized in Tables 8 and 9.

The efficiency scale factors related to lepton identification, isolation, and trigger were applied to each signal simulated sample to correct for observed data and simulation discrepancies. The

uncertainty estimated with the tag and probe technique is found to be of about 1.0%. In order to evaluate the systematic uncertainty related to the tag and probe assumptions, while extracting the efficiencies, the scale factors are increased or decreased at the same time by $\pm 0.5\%$. The global uncertainties was found to be of the order of 2.0% [57].

The pileup systematic uncertainties are evaluated by varying the total inelastic cross-section by $\pm 5\%$. For each variation, the signal yield is recomputed and the maximum difference is taken as systematic uncertainties. The uncertainty was computed separately for GGF and VBF processes, and found to vary depending on the category from a minimum of 0.7% to a maximum of 2.3%.

The b-tag efficiency scale factors applied to the signal as described in Section 6.1 have associated uncertainties. We determine the impact on the overall signal normalization by shifting the scale factors up and down by one sigma. The uncertainty was computed separately for GGF and VBF processes, and found to vary depending on the category from a minimum of 0.05% to a maximum of 0.7%.

The effects of the uncertainties on the jet energy scale and resolution on the selection efficiency was determined using the standard prescription [47] by changing the jet energies and the missing transverse energy of the simulated signal. Table 9 shows the changes in signal yields when varying the jet energy scale and jet energy resolution respectively. The correlations are fully taken into account.

Table 9: Relative change of signal yields when varying the jet energy scale or the jet energy resolution within uncertainties. For reference, the requirement on the number of reconstructed jets is shown in the bottom row.

		Category					
	Process	0	1	2	3	4	5
Jet energy scale	GGF	-10.5%	-8.4%	-7.5%	-11.5%	-15.0%	+0.6%
	VBF	-17.0%	-11.7%	-13.8%	-18.9%	-22.4%	-6.1%
Jet energy resolution	GGF	-13.9%	-8.9%	-3.0%	-12.8%	-10.0%	-0.3%
	VBF	-20.1%	-16.0%	-17.8%	-21.9%	-23.8%	-9.9%
Number of jets		0	1	2	0	1	2

		Category					
	Process	6	7	8		9	10
Jet energy scale	GGF	-10.7%	-15.9%	-3.2%		+26.3%	+77.6%
	VBF	-18.0%	-19.6%	-1.9%		-0.1%	-9.5%
Jet energy resolution	GGF	-13.7%	-9.4%	+3.9%		+31.2%	+93.7%
	VBF	-19.4%	-23.2%	-5.7%		+8.4%	-17.5%
Number of jets		0	1	2		2	2

The systematic uncertainty on the cross section follows the recommendation of the LHC Higgs Cross Section Working Group [59] and amount to up to 10.8%.

Uncertainties on the acceptances due choice of parton distribution function have been taken into account using the PDF4LHC prescription [56] by taking the maximum of the variations over the CT10 [60], MSTW [54] and NNPDF [55] PDF sets.

7 Results

7.1 Limits on branching fraction $B(\mathrm{H} \to \mathrm{e}\tau)$

The $\mathrm{M_{col}}$ distributions the fit of the signal and background contributions are shown in Figure 3 and the event yields in the mass range $100 < \mathrm{M_{col}} < 150\,\mathrm{GeV}$ are shown in Table 10 and Table 11. The categories of the τ_h and τ_μ channels are combined to set a 95% CL upper limit on the branching fraction of LFV Higgs boson decay in $\mathrm{e}\tau$ channel, $B(H \to \mathrm{e}\tau)$.

Table 10: Event yield after the fit in the mass window $100\,\mathrm{GeV} < M_{collinear} < 150\,\mathrm{GeV}$ for the $\mathrm{H} \to \mathrm{e}\tau_h$ channel. The contributions are normalized to an integrated luminosity of 19.7 fb^{-1}. The LFV Higgs boson signal is the MC expectation for $\mathrm{B(H} \to \mathrm{e}\tau) = 1\%$.

Jet category:	0-Jet	1-Jet	2-Jet
Misidentified leptons	3366±25	223±11	8.7± 2.23
$Z \to ee, \mu\mu$	714±30	85±4	3.2± 0.25
$Z \to \tau\tau$	270±10	32±3	1.6± 0.30
$t\bar{t}, t, \bar{t}$	10±2	13±2	0.5± 0.2
EWK diboson	53±2	6±1	0.3± 0.1
SM Higgs boson background	12±1	3±1	1.0± 0.1
Sum of background	4425±28	363±11	15.3±2.3
LFV Higgs boson signal (BR=1%)	88±6	22±2	4.1±0.7
Observed	4438	375	13

Table 11: Event yield after the fit in the mass window $100\,\mathrm{GeV} < M_{collinear} < 150\,\mathrm{GeV}$ for the $\mathrm{H} \to \mathrm{e}\tau_\mu$ channel. The contributions are normalized to an integrated luminosity of 19.7 fb^{-1}. The LFV Higgs boson signal is the MC expectation for $\mathrm{B(H} \to \mathrm{e}\tau) = 1\%$. "-" indicates that 0 MC events for the particular background are selected.

Jet category:	0-Jet	1-Jet	2-Jet
Misidentified leptons	85.2±5.9	38.1±3.9	2.1±0.7
$Z \to ee, \mu\mu$	2.3±0.6	5.4±0.5	-
$Z \to \tau\tau$	84.7±2.1	113.3±4.2	8.5±0.6
$t\bar{t}, t, \bar{t}$	13.8±0.3	69.4±2.3	12.7±0.8
EWK diboson	83.0±2.7	51.7±2.0	3.6±0.4
$W\gamma$, $W\gamma*$	2.2±1.0	1.2±0.6	-
SM Higgs boson background	2.3±0.3	3.6±0.4	1.1±0.2
Sum of background	273.5±6.1	282.0±6.0	28.1±1.3
LFV Higgs boson signal (BR=1%)	33.4±2.3	23.2±1.7	8.6±1.4
Observed	286	268	33

Table 12 reports the observed and the mean expected 95% CL upper limits on the $B(H \to \mathrm{e}\tau)$ for Higgs boson mass at 125 GeV for each category of the $\mathrm{H} \to \mathrm{e}\tau_h$ and $\mathrm{H} \to \mathrm{e}\tau_\mu$ channels. Combining the two channels an expected upper limit of $B(\mathrm{H} \to \mathrm{e}\tau) < (0.75 \pm 0.39)\%$ is obtained. The observed upper limit is $B(\mathrm{H} \to \mathrm{e}\tau) < 0.69\%$. The limits are also summarized graphically in Figure 4. The fit can then be used to estimate the branching fraction. The best fit values for the branching fractions are given in Table 12. The combined categories give a null best fit branching fraction.

Table 12: The expected upper limits, observed limits and best fit values for the branching fractions $B(\mathrm{H} \to \mathrm{e}\tau)$ for different jet categories and analysis channels. The one standard-deviation probability intervals around the expected limits are shown in parentheses.

Expected Limits			
	0 Jet (%)	1 Jet (%)	2 Jets (%)
$e\tau_\mu$	$< 1.63(^{+0.66}_{-0.44})$	$< 1.54(^{+0.71}_{-0.47})$	$< 1.59(^{+0.93}_{-0.55})$
$e\tau_h$	$< 2.71^{+1.05}_{-0.75}$	$< 2.76^{+1.07}_{-0.77}$	$< 3.55^{+1.38}_{-0.99}$
$e\tau$	$< 0.75(^{+0.32}_{-0.22})$		
Observed Limits			
	0 Jet (%)	1 Jet (%)	2 Jets (%)
$e\tau_\mu$	< 1.83	< 0.94	< 1.49
$e\tau_h$	< 3.92	< 3.00	< 2.88
$e\tau$	< 0.69		
Best Fit Branching Fractions			
	0 Jet (%)	1 Jet (%)	2 Jets (%)
$e\tau_\mu$	$0.19^{+0.85}_{-0.85}$	$-1.04^{+0.70}_{-0.70}$	$-0.12^{+0.67}_{-0.58}$
$e\tau_h$	$1.43^{+1.38}_{-1.33}$	$0.30^{+1.37}_{-1.38}$	$-0.91^{+1.54}_{-1.57}$
$e\tau$	$-0.10^{+0.37}_{-0.36}$		

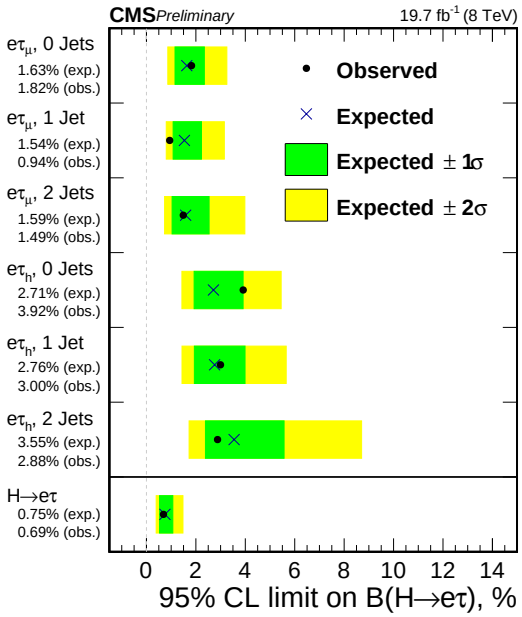

Figure 4: Upper limits by category for the LFV $\mathrm{H} \to \mathrm{e}\tau$ decays.

7.2 Limits on lepton-flavour-violating couplings $|Y_{e\tau}|$ and $|Y_{\tau e}|$

The constraint on $B(\mathrm{H} \to \mathrm{e}\tau)$ can be interpreted in terms of LFV Higgs boson Yukawa couplings [3]. The LFV decays $H \to e\mu, e\tau_h, \mathrm{e}\tau_\mu$ arise at tree level from the assumed flavour violating Yukawa interactions, $Y_{\ell^\alpha \ell^\beta}$ where ℓ^α, ℓ^β denote the leptons, $\ell^\alpha, \ell^\beta = \mathrm{e}, \mu, \tau$ and $\ell^\alpha \neq \ell^\beta$. The decay width $\Gamma(\mathrm{H} \to \ell^\alpha \ell^\beta)$ in terms of the Yukawa couplings is given by:

$$\Gamma(\mathrm{H} \to \ell^\alpha \ell^\beta) = \frac{m_H}{8\pi}(|Y_{\ell^\beta \ell^\alpha}|^2 + |Y_{\ell^\alpha \ell^\beta}|^2),$$

and the branching fraction by:

$$B(H \to \ell^\alpha \ell^\beta) = \frac{\Gamma(H \to \ell^\alpha \ell^\beta)}{\Gamma(H \to \ell^\alpha \ell^\beta) + \Gamma_{SM}}.$$

The SM Higgs boson decay width is $\Gamma_{SM} = 4.1$ MeV for a 125 GeV Higgs boson. The 95%

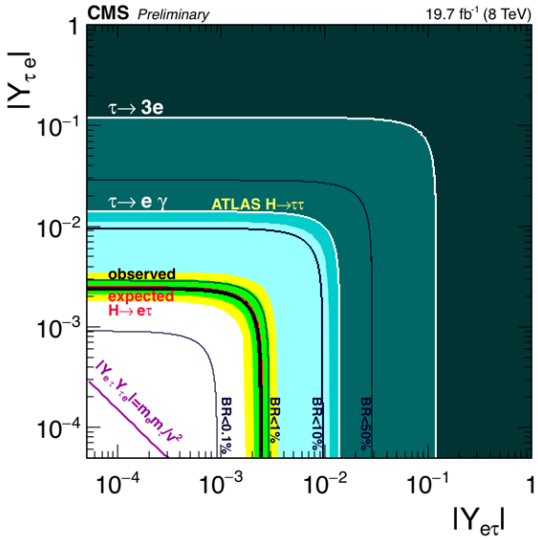

Figure 5: Constraints on the flavour violating Yukawa couplings, $|Y_{\mathrm{e}\tau}|, |Y_{\tau\mathrm{e}}|$. The expected (red solid line) and observed (black solid line) limits are derived from the limit on $B(\mathrm{H} \to \mathrm{e}\tau)$ from the present analysis. The flavour diagonal Yukawa couplings are approximated by their SM values. The green (yellow) band indicates the range that is expected to contain 68% (95%) of all observed limit excursions from the expected limit. The shaded regions are derived constraints from null searches for $\tau \to 3\mathrm{e}$ (dark green) and $\tau \to \mathrm{e}\gamma$ (lighter green). The purple diagonal line is the theoretical naturalness limit $Y_{ij}Y_{ji} \leq m_i m_j / v^2$. The yellow line is the limit from a theoretical reinterpretation of an ATLAS $\mathrm{H} \to \tau\tau$ search [3].

confidence level constraint on the Yukawa couplings derived from $B(\mathrm{H} \to \mathrm{e}\tau) < 0.69\%$ and the expression for the branching fraction above is:

$$\sqrt{|Y_{\mathrm{e}\tau}|^2 + |Y_{\tau\mathrm{e}}|^2} < 2.41 \times 10^{-3}.$$

Figure 5 compares this result to the constraints from previous indirect measurements.

7.3 Limits on branching fraction $B(\mathrm{H} \to \mathrm{e}\mu)$

The event yields, after the selection described in Sec. 6.1, in the mass range $124 < m_{e\mu} < 126$ GeV are shown in Table 13 separately for simulation and observed data. The observed mass spectra for various groups of categories are shown in Figure 6.

Table 13: Event yields in the mass window 124 GeV $< m_{e\mu} <$ 126 GeV for the H $\to$ eμ channel. The expected contributions are normalized to an integrated luminosity of 19.7 fb^{-1}. The LFV Higgs boson signal is the MC expectation for B(H $\to$ eμ = 0.1%).

Jet category:	0-Jet	1-Jet	2-Jet	VBF
Drell-Yan	17.8 ± 4.2	4.1 ± 2.0	1.9 ± 1.4	0.0 ± 0.0
$t\bar{t}$	1.4 ± 1.2	3.1 ± 1.8	14.1 ± 3.8	0.4 ± 0.6
t, $\bar{t}$	0.0 ± 0.0	0.0 ± 0.0	2.7 ± 1.6	0.0 ± 0.0
EWK diboson	21.6 ± 4.7	2.3 ± 0.2	0.0 ± 0.0	0.0 ± 0.0
SM Higgs boson background	0.0 ± 0.0	0.1 ± 0.2	0.0 ± 0.0	0.0 ± 0.0
Sum of backgrounds	40.8 ± 6.4	9.6 ± 3.1	18.8 ± 4.3	0.5 ± 0.7
Observed	49	6	17	2
(Data-BG)/Uncert(BG)	1.3	-1.2	-0.4	2.2
LFV Higgs boson signal (B=1%)	21.2 ± 4.6	9.1 ± 3.0	2.6 ± 1.6	1.5 ± 1.2

No siginifcant excess over the expected background is observed. The exclusion limit on the branching ratio H $\to$ eμ as a function of the Higgs boson mass hypothesis has been derived using the CLs asymptotic model [61]. The values of the exclusion for a Higgs boson mass hypothesis of $m_{\mathrm{H}} = 125\,\mathrm{GeV}$ are given shown in Figure 7 for the inclusive categories grouped by number of jets, the VBF categories and all all categories combined.

7.4 Limits on lepton-flavour-violating couplings $|Y_{e\mu}|$ and $|Y_{\mu e}|$

As done in sec. 7.2 the constraint on $B(\mathrm{H} \to \mathrm{e}\mu)$ can be reintepreted in terms of upper limits on Yukawa coupling. Following the equation in sec. 7.2, the observed 95% confidence level upper limit on the Yukawa coupling derived from $B(\mathrm{H} \to \mathrm{e}\mu) < 3.6 \times 10^{-4}$ is:

$$\sqrt{|Y_{e\mu}|^2 + |Y_{\mu e}|^2} < 5.43 \times 10^{-4}.$$

Figure 8 compares this result to the constraints from previous indirect measurements. From the absence of $\mu \to \mathrm{e}\gamma$ decays, a limit of $\sqrt{|Y_{e\mu}|^2 + |Y_{\mu e}|^2} < 3.6 \times 10^{-6}$ is obtained in [3] under the assumption that flavour-changing neutral currents are dominated by the Higgs boson contributions The authors mention however explicitly that in general, flavour violation induced by the Higgs boson can be cancelled by flavour violation generated by other new physics. The direct search for H $\to$ eμ decays presented here is thus complementary to indirect limits obtained from searches for rare decays at lower energies.

8 Conclusions

The first direct search for lepton-flavour-violating decays of a Higgs boson, based on the full 8 TeV dataset collected by CMS in 2012, is presented. The search of the H $\to$ eτ decay improves upon previously published indirect limits [3, 22] by an order of magnitude. A observed upper limit of $B(\mathrm{H} \to \mathrm{e}\tau) < 0.7\%$ at 95% confidence level is found. The limit is used to constrain the $Y_{\mathrm{e}\tau}$ Yukawa coupling. It improves the current bound by an order of magnitude.
The search of the H $\to$ eμ decay has been performed for different Higgs boson mass hypotheses and leads to the observed upper limit of $B(\mathrm{H} \to \mathrm{e}\mu) < 0.036\%$ at 95% confidence level. Interpreting this limit in terms of Yukawa coupling, the upper limit is of the order of $O(10^{-4})$ at 95% confidence level.

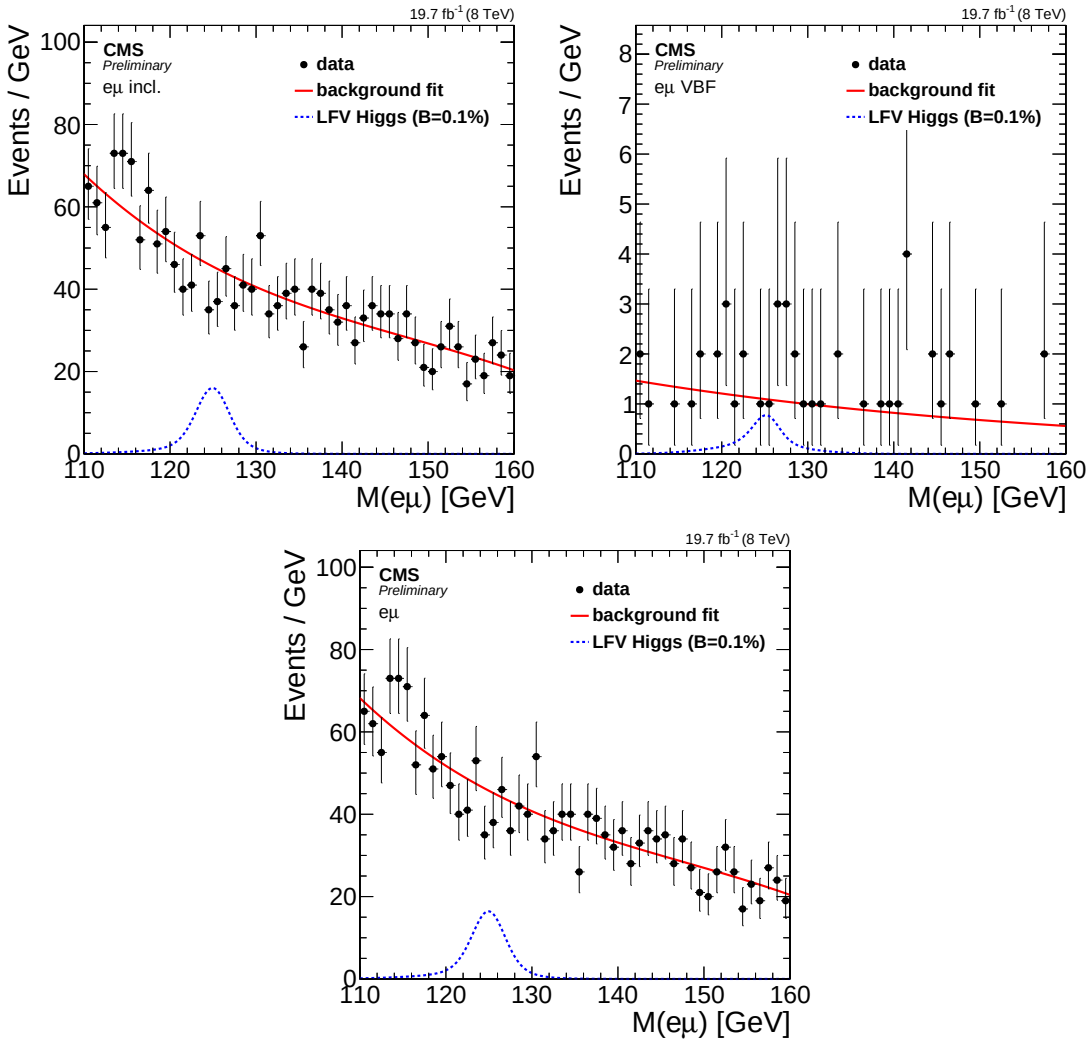

Figure 6: Observed eμ mass spectra (points), background fit (solid line) and signal model (blue histogram) for BR(H $\rightarrow$ eμ) = 0.1%. The top plots shows the results for the inclusive (left) and jet tagged (right) categories while the bottom plot shows the combination of all categories.

9 Acknowledgements

We congratulate our colleagues in the CERN accelerator departments for the excellent performance of the LHC and thank the technical and administrative staffs at CERN and at other CMS institutes for their contributions to the success of the CMS effort. In addition, we gratefully acknowledge the computing centres and personnel of the Worldwide LHC Computing Grid for delivering so effectively the computing infrastructure essential to our analyses. Finally, we acknowledge the enduring support for the construction and operation of the LHC and the CMS detector provided by the following funding agencies: BMWFW and FWF (Austria); FNRS and FWO (Belgium); CNPq, CAPES, FAPERJ, and FAPESP (Brazil); MES (Bulgaria); CERN; CAS, MoST, and NSFC (China); COLCIENCIAS (Colombia); MSES and CSF (Croatia); RPF (Cyprus); MoER, ERC IUT and ERDF (Estonia); Academy of Finland, MEC, and HIP (Finland); CEA and CNRS/IN2P3 (France); BMBF, DFG, and HGF (Germany); GSRT (Greece); OTKA and NIH (Hungary); DAE and DST (India); IPM (Iran); SFI (Ireland); INFN (Italy); NRF and WCU (Republic of Korea); LAS (Lithuania); MOE and UM (Malaysia); CINVESTAV, CONACYT, SEP, and UASLP-FAI (Mexico); MBIE (New Zealand); PAEC (Pakistan); MSHE and NSC (Poland);

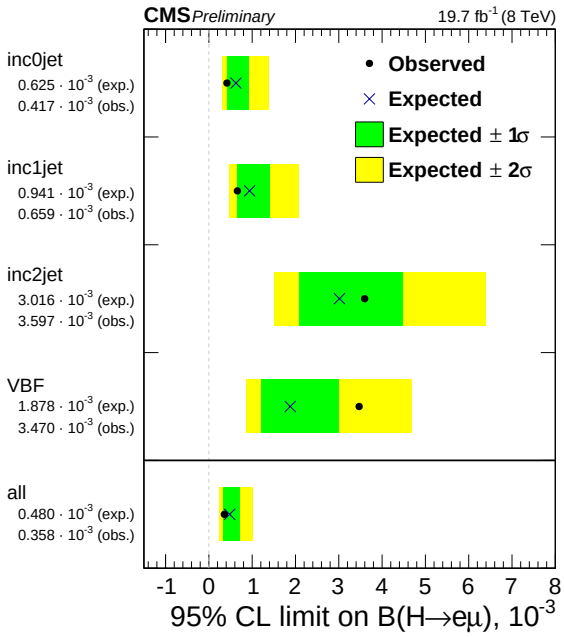

Figure 7: Upper limit on BR(H $\rightarrow$ eμ) at M_{H}= 125 GeV for inclusive categories grouped by number of jets, jet tagged and all categories combined.

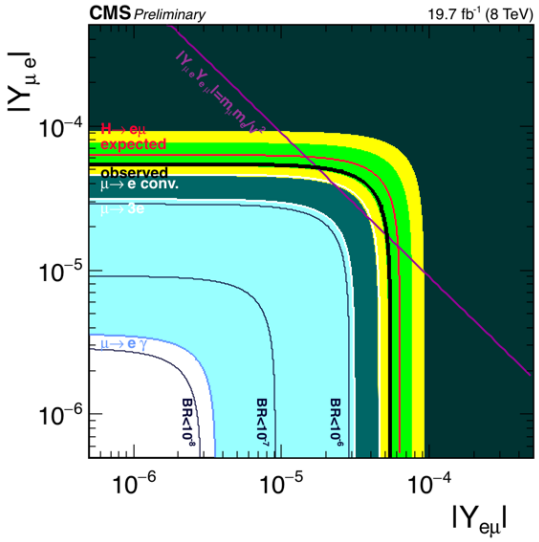

Figure 8: Constraints on the flavour violating Yukawa couplings, $|Y_{\mathrm{e}\mu}|, |Y_{\mu\mathrm{e}}|$. The expected (red solid line) and observed (black solid line) limits are derived from the limit on $B(\mathrm{H} \rightarrow \mathrm{e}\mu)$ from the present analysis. The flavour diagonal Yukawa couplings are approximated by their SM values. The green (yellow) band indicates the range that is expected to contain 68% (95%) of all observed limit excursions from the expected limit. The shaded regions are derived constraints from null searches for $\mu \rightarrow$ e conversion (dark green), $\mu \rightarrow$ 3e (light green), and $\tau \rightarrow \mathrm{e}\gamma$ (cyan). The purple diagonal line is the theoretical naturalness limit $Y_{ij}Y_{ji} \leq m_i m_j / v^2$.

FCT (Portugal); JINR (Dubna); MON, RosAtom, RAS and RFBR (Russia); MESTD (Serbia); SEIDI and CPAN (Spain); Swiss Funding Agencies (Switzerland); MST (Taipei); ThEPCenter, IPST, STAR and NSTDA (Thailand); TUBITAK and TAEK (Turkey); NASU and SFFR (Ukraine); STFC (United Kingdom); DOE and NSF (USA). Individuals have received support from the MarieCurie programme and the European Research Council (European Union); the Leventis Foundation; the A.P. Sloan Foundation; the Alexander von Humboldt Foundation; the Belgian Federal Science Policy Office; the Fonds pour la Formation la Recherche dans lIndustrie et dans lAgriculture (FRIA-Belgium); the Agentschap voor Innovatie door Wetenschap en Technologie (IWT-Belgium); and the Council of Science and Industrial Research, India.

References

[1] CMS Collaboration, "Observation of a new boson at a mass of 125 GeV with the CMS experiment at the LHC", *Phys. Lett.* **B716** (2012) 30–61, doi:10.1016/j.physletb.2012.08.021, arXiv:1207.7235.

[2] ATLAS Collaboration, "Observation of a new particle in the search for the Standard Model Higgs boson with the ATLAS detector at the LHC", *Phys. Lett.* **B716** (2012) 1–29, doi:10.1016/j.physletb.2012.08.020, arXiv:1207.7214.

[3] R. Harnik, J. Kopp, and J. Zupan, "Flavor Violating Higgs Decays", *JHEP* **1303** (2013) 026, doi:10.1007/JHEP03(2013)026, arXiv:1209.1397.

[4] J. D. Bjorken and S. Weinberg, "Mechanism for Nonconservation of Muon Number", *Phys. Rev. Lett.* **38** (Mar, 1977) 622–625, doi:10.1103/PhysRevLett.38.622.

[5] J. L. Diaz-Cruz and J. Toscano, "Lepton flavor violating decays of Higgs bosons beyond the standard model", *Phys. Rev.* **D62** (2000) 116005, doi:10.1103/PhysRevD.62.116005, arXiv:hep-ph/9910233.

[6] T. Han and D. Marfatia, "$h \to \mu\tau$ at hadron colliders", *Phys. Rev. Lett.* **86** (2001) 1442–1445, doi:10.1103/PhysRevLett.86.1442, arXiv:hep-ph/0008141.

[7] A. Arhrib, Y. Cheng, and O. C. Kong, "A Comprehensive Analysis on Lepton Flavor Violating Higgs to $\mu\bar{\tau} + \tau\bar{\mu}$ Decay in Supersymmetry without R Parity", *Phys. Rev.* **D87** (2013) 015025, doi:10.1103/PhysRevD.87.015025, arXiv:1210.8241.

[8] K. Agashe and R. Contino, "Composite Higgs-Mediated FCNC", *Phys. Rev.* **D80** (2009) 075016, doi:10.1103/PhysRevD.80.075016, arXiv:0906.1542.

[9] A. Azatov, M. Toharia, and L. Zhu, "Higgs Mediated FCNC's in Warped Extra Dimensions", *Phys. Rev.* **D80** (2009) 035016, doi:10.1103/PhysRevD.80.035016, arXiv:0906.1990.

[10] H. Ishimori et al., "Non-Abelian Discrete Symmetries in Particle Physics", *Prog.Theor.Phys.Suppl.* **183** (2010) 1–163, doi:10.1143/PTPS.183.1, arXiv:1003.3552.

[11] G. Perez and L. Randall, "Natural Neutrino Masses and Mixings from Warped Geometry", *JHEP* **0901** (2009) 077, doi:10.1088/1126-6708/2009/01/077, arXiv:0805.4652.

[12] S. Casagrande et al., "Flavor Physics in the Randall-Sundrum Model: I. Theoretical Setup and Electroweak Precision Tests", *JHEP* **0810** (2008) 094, doi:10.1088/1126-6708/2008/10/094, arXiv:0807.4937.

[13] A. J. Buras, B. Duling, and S. Gori, "The Impact of Kaluza-Klein Fermions on Standard Model Fermion Couplings in a RS Model with Custodial Protection", *JHEP* **0909** (2009) 076, doi:10.1088/1126-6708/2009/09/076, arXiv:0905.2318.

[14] M. Blanke et al., "$\Delta F = 2$ Observables and Fine-Tuning in a Warped Extra Dimension with Custodial Protection", *JHEP* **0903** (2009) 001, doi:10.1088/1126-6708/2009/03/001, arXiv:0809.1073.

[15] G. F. Giudice and O. Lebedev, "Higgs-dependent Yukawa couplings", *Phys. Lett.* **B665** (2008) 79–85, doi:10.1016/j.physletb.2008.05.062, arXiv:0804.1753.

[16] J. Aguilar-Saavedra, "A Minimal set of top-Higgs anomalous couplings", *Nucl. Phys.* **B821** (2009) 215–227, doi:10.1016/j.nuclphysb.2009.06.022, arXiv:0904.2387.

[17] M. E. Albrecht et al., "Electroweak and Flavour Structure of a Warped Extra Dimension with Custodial Protection", *JHEP* **0909** (2009) 064, doi:10.1088/1126-6708/2009/09/064, arXiv:0903.2415.

[18] A. Goudelis, O. Lebedev, and J. H. Park, "Higgs-induced lepton flavor violation", *Phys. Lett.* **B707** (2012) 369–374, doi:10.1016/j.physletb.2011.12.059, arXiv:1111.1715.

[19] D. McKeen, M. Pospelov, and A. Ritz, "Modified Higgs branching ratios versus CP and lepton flavor violation", *Phys. Rev.* **D86** (2012) 113004, doi:10.1103/PhysRevD.86.113004, arXiv:1208.4597.

[20] B. McWilliams and L.-F. Li, "Virtual Effects of Higgs Particles", *Nucl. Phys.* **B179** (1981) 62, doi:10.1016/0550-3213(81)90249-2.

[21] O. U. Shanker, "Flavor Violation, Scalar Particles and Leptoquarks", *Nucl. Phys.* **B206** (1982) 253, doi:10.1016/0550-3213(82)90534-X.

[22] G. Blankenburg, J. Ellis, and G. Isidori, "Flavour-Changing Decays of a 125 GeV Higgs-like Particle", *Phys. Lett.* **B712** (2012) 386–390, doi:10.1016/j.physletb.2012.05.007, arXiv:1202.5704.

[23] Particle Data Group Collaboration, "Review of Particle Physics (RPP)", *Phys. Rev.* **D86** (2012) 010001, doi:10.1103/PhysRevD.86.010001.

[24] S. Kanemura, T. Ota, and K. Tsumura, "Lepton flavor violation in Higgs boson decays under the rare tau decay results", *Phys. Rev.* **D73** (2006) 016006, doi:10.1103/PhysRevD.73.016006, arXiv:hep-ph/0505191.

[25] S. Davidson and G. J. Grenier, "Lepton flavour violating Higgs and tau to mu gamma", *Phys. Rev.* **D81** (2010) 095016, doi:10.1103/PhysRevD.81.095016, arXiv:1001.0434.

[26] A. Celis, V. Cirigliano, and E. Passemar, "Lepton flavor violation in the Higgs sector and the role of hadronic tau-lepton decays", *Phys. Rev.* **D89** (2014) 013008, doi:10.1103/PhysRevD.89.013008, arXiv:1309.3564.

[27] S. M. Barr and A. Zee, "Electric Dipole Moment of the Electron and of the Neutron", *Phys. Rev. Lett.* **65** (1990) 21–24, doi:10.1103/PhysRevLett.65.21.

[28] CMS Collaboration, "Search for lepton-flavour-violating decays of the Higgs boson", arXiv:1502.07400.

[29] CMS Collaboration, "Evidence for the direct decay of the 125 GeV Higgs boson to fermions", *Nature Phys.* **10** (2014) doi:10.1038/nphys3005, arXiv:1401.6527.

[30] CMS Collaboration, "Evidence for the 125 GeV Higgs boson decaying to a pair of τ leptons", *J. High Energy Phys.* **05** (2014) 104, doi:10.1007/JHEP05(2014)104.

[31] T. Junk, "Confidence level computation for combining searches with small statistics", *Nucl. Instrum. Meth. A* **434** (1999) 435, doi:10.1016/S0168-9002(99)00498-2, arXiv:hep-ex/9902006.

[32] A. L. Read, "Presentation of search results: the CL_s technique", *J. Phys. G* **28** (2002) 2693, doi:10.1088/0954-3899/28/10/313.

[33] CMS Collaboration, "The CMS experiment at the CERN LHC", *JINST* **3** (2008) S08004, doi:10.1088/1748-0221/3/08/S08004.

[34] GEANT4 Collaboration, "GEANT4—a simulation toolkit", *Nucl. Instrum. Meth. A* **506** (2003) 250, doi:10.1016/S0168-9002(03)01368-8.

[35] T. Sjöstrand, S. Mrenna, and P. Skands, "A Brief Introduction to PYTHIA 8.1", (2007) arXiv:0710.3820.

[36] Sjostrand, T. and Mrenna, S. and Skands, P., "PYTHIA 6.4: Physics and Manual", arXiv:0603175.

[37] LHC Higgs Cross Section Working Group et al., "Handbook of LHC Higgs Cross Sections: 1. Inclusive Observables", *CERN-2011-002* (CERN, Geneva, 2011) arXiv:1101.0593.

[38] J. Alwall et al., "MadGraph 5 : Going Beyond", *JHEP* **1106** (2011) 128, doi:10.1007/JHEP06(2011)128, arXiv:1106.0522.

[39] CMS Collaboration, "Particle–Flow Event Reconstruction in CMS and Performance for Jets, Taus, a nd $E_{\mathrm{T}}^{\mathrm{miss}}$", *CMS Physics Analysis Summary* **CMS-PAS-PFT-09-001** (2009).

[40] CMS Collaboration, "Commissioning of the Particle-Flow Reconstruction in Minimum-Bias and Jet Even ts from pp Collisions at 7 TeV", *CMS Physics Analysis Summary* **CMS-PAS-PFT-10-002** (2010).

[41] CMS Collaboration, "Commissioning of the particle–flow event reconstruction with leptons from J/ψ and W decays at 7 TeV", *CMS Physics Analysis Summary* **CMS-PAS-PFT-10-003** (2010).

[42] K. Rose, "Deterministic Annealing for Clustering, Compression, Classification, Regression and related Optimisation Problems", *Proceedings of the IEEE* **Vol. 86, Issue 11** (1998).

[43] CMS Collaboration, "Performance of CMS muon reconstruction in pp collision events at $\sqrt{s} = 7$ TeV", *JINST* **7** (2012) P10002, doi:10.1088/1748-0221/7/10/P10002, arXiv:1206.4071.

[44] CMS Collaboration, "Properties of the Higgs-like boson in the decay $H \to ZZ \to 4\ell$ in pp collisions at $\sqrt{s} = 7$ and 8 TeV", *CMS Physics Analysis Summary* **CMS-PAS-HIG-13-002** (2013).

[45] M. Cacciari, G. P. Salam, "Dispelling the N^3 myth for the k_t jet-finder", *Phys. Lett. B* **641** (2006) 57, doi:10.1016/j.physletb.2006.08.037, arXiv:hep-ph/0512210.

[46] M. Cacciari, G. P. Salam, and G. Soyez, "The anti-k_t jet clustering algorithm", *JHEP* **04** (2008) 063, doi:10.1088/1126-6708/2008/04/063, arXiv:0802.1189.

[47] CMS Collaboration, "Determination of jet energy calibration and transverse momentum resolution in CMS", *JINST* **6** (2011) 11002, doi:10.1088/1748-0221/6/11/P11002, arXiv:1107.4277.

[48] CMS Collaboration, "Pileup Jet Identification", *CMS Physics Analysis Summary* **CMS-PAS-JME-13-005** (2013).

[49] CMS Collaboration, "Performance of tau-lepton reconstruction and identification in CMS", *JINST* **7** (2012) P01001, doi:10.1088/1748-0221/7/01/P01001, arXiv:1109.6034.

[50] R. K. Ellis, I. Hinchliffe, M. Soldate, and J. van der Bij, "Higgs Decay to tau+ tau-: A Possible Signature of Intermediate Mass Higgs Bosons at the SSC", *Nucl. Phys.* **B297** (1988) 221, doi:10.1016/0550-3213(88)90019-3.

[51] CMS Collaboration, "Identification of b-quark jets with the CMS experiment", *JINST* **8** (2012) P04013, doi:10.1088/1748-0221/8/04/P04013.

[52] CMS Collaboration Collaboration, "Measurement of the Inclusive W and Z Production Cross Sections in pp Collisions at $\sqrt{s} = 7$ TeV", *JHEP* **10** (2011) 132, doi:10.1007/JHEP10(2011)132, arXiv:1107.4789.

[53] P. M. Nadolsky et al., "Implications of CTEQ global analysis for collider observables", *Phys. Rev.* **D78** (2008) 013004, doi:10.1103/PhysRevD.78.013004, arXiv:0802.0007.

[54] A. Martin, W. Stirling, R. Thorne, and G. Watt, "Parton distributions for the LHC", *Eur. Phys. J.* **C63** (2009) 189–285, doi:10.1140/epjc/s10052-009-1072-5, arXiv:0901.0002.

[55] R. D. Ball et al., "A first unbiased global NLO determination of parton distributions and their uncertainties", *Nucl. Phys.* **B838** (2010) 136–206, doi:10.1016/j.nuclphysb.2010.05.008, arXiv:1002.4407.

[56] M. Botje et al., "The PDF4LHC Working Group Interim Recommendations", (2011). arXiv:1101.0538.

[57] CMS Collaboration, "Observation of the diphoton decay of the Higgs boson and measurement of its properties", *The European Physical Journal C* **74** (2014), no. 10, doi:10.1140/epjc/s10052-014-3076-z.

[58] CMS Collaboration, "Performance of b tagging at sqrt(s)=8 TeV in multijet, ttbar and boosted topology events", *CMS Physics Analysis Summary* **CMS-PAS-BTV-13-001** (2013).

[59] LHC Higgs Cross Section Working Group, "Handbook of LHC Higgs cross sections: 3. Higgs Properties", CERN Report CERN-2013-004, 2013. doi:10.5170/CERN-2013-004, arXiv:1307.1347.

[60] H.-L. Lai et al., "New parton distributions for collider physics", *Phys. Rev. D* **82** (2010) 074024, doi:10.1103/PhysRevD.82.074024, arXiv:1007.2241.

[61] G. Cowan, K. Cranmer, E. Gross, and O. Vitells, "Asymptotic formulae for likelihood-based tests of new physics", *The European Physical Journal C* **71** (2011), no. 2, doi:10.1140/epjc/s10052-011-1554-0.